Reduction of the thermocline feedback associated with mean SST bias in ENSO simulation

Baoqiang Xiang · Bin Wang · Qinghua Ding ·
Fei–Fei Jin · Xiouhua Fu · Hyung-Jin Kim

Abstract Associated with the double Inter-tropical convergence zone problem, a dipole SST bias pattern (cold in the equatorial central Pacific and warm in the southeast tropical Pacific) remains a common problem inherent in many contemporary coupled models. Based on a newly-developed coupled model, we performed a control run and two sensitivity runs, one is a coupled run with annual mean SST correction and the other is an ocean forced run. By comparison of these three runs, we demonstrated that a serious consequence of this SST bias is to severely suppress the thermocline feedback in a realistic simulation of the El Niño/Southern Oscillation. Firstly, the excessive cold tongue extension pushes the anomalous convection far westward from the equatorial central Pacific, prominently diminishing the convection-low level wind feedback and thus the air-sea coupling strength. Secondly, the equatorial surface wind anomaly exhibits a relatively uniform meridional structure with weak gradient, contributing to a weakened wind-thermocline feedback. Thirdly, the equatorial cold SST bias induces a weakened upper-ocean stratification and thus yields the underestimation of the thermocline-subsurface temperature feedback. Finally, the dipole SST bias underestimates the mean upwelling through (a) undermining equatorial mean easterly wind stress, and (b) enhancing convective mixing and thus reducing the upper ocean stratification, which weakens vertical shear of meridional currents and near-surface Ekman-divergence.

Keywords ENSO · SST bias · Thermocline feedback · Air-sea coupling

B. Xiang (✉) · B. Wang · Fei–Fei Jin
Department of Meteorology, School of Ocean and Earth Science
and Technology, University of Hawaii at Manoa,
2525 Correa Rd., HIG 350, Honolulu, HI 96822, USA
e-mail: baoqiang@hawaii.edu

B. Wang · X. Fu
International Pacific Research Center,
University of Hawaii at Manoa, Honolulu, HI 96822, USA

Q. Ding
Department of Earth and Space Sciences, Quaternary Research
Center, University of Washington, Seattle, WA 98195, USA

H.-J. Kim
Research Institute for Global Change,
Japan Agency for Marine-Earth Science and Technology,
3173-25 Showa-machi, Kanazawa-ku, Yokohama,
Kanagawa 236-0001, Japan

1 Introduction

The simulation of El Niño/Southern Oscillation (ENSO) in the coupled General Circulation Models (CGCMs) has achieved steady progresses in recent decades (Mechoso et al. 1995; Latif et al. 2001; AchutaRao and Sperber 2002; Meehl et al. 2005; Randall et al. 2007). However, the simulated ENSO characteristics in terms of amplitude, period, irregularity, skewness and spatial pattern, still remain unrealistic in various degrees (e.g., Guilyardi 2006; AchutaRao and Sperber 2006; Guilyardi et al. 2009b). Understanding and improving ENSO simulation is of particular importance and highly desirable for a number of reasons. Firstly, the reality of ENSO representation seriously affects the skill and confidence of climate predictability from synoptic to interannual time scales (e.g., Vitart et al. 2003; Guldberg et al. 2005). Secondly, the diverse (or even opposite) results on the projected changes of ENSO properties in response to anthropogenic forcing (Merryfield 2006; Guilyardi 2006; Philip and van Oldenborgh 2006; Latif and Keenlyside 2009; Kim and Jin 2010) are more

often attributable to the notorious deficiencies in representing ENSO under the present-day climate. Thirdly, realistic ENSO simulation largely determines the capability and fidelity of a model in reproducing the most prominent tropical and tropical-extratropical teleconnections (e.g., Joseph and Nigam 2006).

Diagnosing the possible sources of systematic biases is an essential step to understand and alleviate these biases in ENSO simulation. Usually, systematic biases in a coupled system can be traced back to shortcomings of individual model components. For example, the convection scheme in an atmospheric model has been known to have profound influences on ENSO simulation in a coupled system (Kim et al. 2008; Neale et al. 2008; Guilyardi et al. 2009a). From the oceanic point of view, Meehl et al. (2001) highlighted the importance of vertical diffusivity and claimed that weaker vertical diffusivity is able to produce stronger ENSO amplitude due to the resultant sharp thermocline gradients. Another essential process is the atmosphere–ocean feedback that may exacerbate any model's intrinsic biases and further cause a mean-state drift away from the observed climate, which, in turn, will also affect ENSO simulation.

The strong interactions between annual mean state and ENSO have been extensively investigated in previous studies in both observations and numerical models (e.g., Li and Hogan 1999; Fedorov and Philander 2000; Wang and An 2001; An et al. 2010). By the same token, the mean state biases in a coupled system could undermine the quality of ENSO simulation (Wittenberg et al. 2006; Large and Danabasoglu 2006; Spencer et al. 2007; Manganello and Huang 2009). Spencer et al. (2007) suggested that ENSO amplitude is very sensitive to not only the heat flux corrections imposed but also the applied meridional extent of it (i.e., tropical vs. equatorial regions). Manganello and Huang (2009) pointed out that the warm SST bias in the Southeast Pacific (SEP) tends to induce a stronger ENSO amplitude. Kim and Jin (2010) investigated the ENSO simulated by the CGCMs from Intergovernmental Panel on Climate Change (IPCC) Fourth Assessment Report (AR4) and concluded that the majority of current CGCMs underestimate the thermocline feedback, which is particularly ascribable to the weak air-sea coupling strength and mean upwelling in the equatorial Pacific.

As the dominant factor controlling the development of ENSO events, weakened thermocline feedback will reduce the simulated ENSO amplitude. Meanwhile, it may also alter the periodicity of ENSO. Previous studies have shown that the time scale of ENSO is primarily determined by the relative contribution from the thermocline feedback and the zonal advection feedback (An and Jin 2001), so that a weaker thermocline feedback favors a relatively shorter ENSO cycle, and vice versa. Therefore, investigating the

cause of the weak thermocline feedback is of particular importance to improve the ENSO simulation. However, to the best of our knowledge, this has not been systematically addressed in the literature. In this study, we aim to investigate how the mean SST bias influences the thermocline feedback. The finding of this study is expected to guide the improvement of atmosphere–ocean models in terms of better ENSO simulation, and may also provide important clues applicable to the study of ENSO property changes in a future warmer climate.

This paper is organized as follows. Section 2 gives a brief description of model components, coupling strategies, experiments, and datasets used in this study. The coupled mean state and ENSO properties are described in Sect. 3. Sections 4 and 5 investigate the impacts of mean SST bias on air-sea coupling strength, wind-thermocline and thermocline-subsurface temperature coupling, respectively. The dynamic and thermodynamic processes associated with mean SST bias that leads to weak mean upwelling are discussed in Sect. 6. Section 7 summaries our major findings and discusses remained issues.

2 Model description, experiments and validation datasets

A coupled model has been developed. The ocean model is the Parallel Ocean Program (POP, v2.0) model (Smith et al. 1992; Dukowicz and Smith 1994). The atmospheric model is the Max-Planck-Institute (MPI) ECHAM (v4.6) model (Roeckner et al. 1996). They have been coupled via the Ocean–Atmosphere-Sea Ice-Soil (OASIS, v3.0) coupler (Valcke et al. 2003). For convenience, hereinafter we refer to it as the POEM coupled model. Each component of this coupled system is briefly described in this section.

2.1 The POP ocean model

The POP (v2.0) ocean model is developed at Los Alamos National Laboratory (Smith et al. 1992; Dukowicz and Smith 1994). This model is a Bryan-Cox-type, level-coordinated model with Boussinesq approximation. The model solves the primitive equations in general orthogonal coordinates in the horizontal direction subject to the hydrostatic approximation. The barotropic equation is solved by using a linearized, implicitly free-surface formulation. The Gent and McWilliams (1990) horizontal isopycnal transport scheme is adopted for tracer equations. The momentum equations use the anisotropic horizontal viscosity. The K-profile parameterization (KPP, Large et al. 1994) is used to determine vertical mixing.

The KPP scheme adopts two different turbulence models within ocean boundary layer and ocean interior, and

these two models are coupled through continuity of turbulence diffusivities and their derivatives at the base of the boundary layer (Large et al. 1997). The vertical viscosity is a factor of 10 (the Prandtl number) larger than diffusivity. Within the ocean boundary layer, the turbulence diffusivities are parameterized by cubic functions with coefficients determined by surface wind stress, buoyancy flux, and boundary conditions at the base of the boundary layer (Large et al. 1997). Below the surface boundary layer, the vertical fluxes follow the downgradient transport hypothesis, with turbulence diffusivities being expressed as the superposition of the contributions from shear-driven mixing, internal waves breaking, double diffusion, and molecular diffusion (Large et al. 1997).

The basic model configuration for the POP model is borrowed from a low resolution version of CCSM3 (Community Climate System Model) model (Yeager et al. 2006), with horizontal 100 (zonal) × 116 (meridional) grid points (meridionally about 0.6° in the near equatorial region) and 25 vertical levels. The vertical resolution is about 10 m at the upper 100 m. We also embedded a solar absorption component based on specified monthly mean surface chlorophyll concentration (Ohlmann 2003) that is also borrowed from CCSM3.

2.2 The ECHAM atmospheric model

The prognostic variables in the ECHAM (v4.6) model include vorticity, divergence, temperature, surface pressure, water vapor, and cloud water. The surface fluxes of momentum, heat, water vapor and cloud water are calculated based on the Monin–Obukhov similarity theory. The vertical diffusion in the model is computed with a high order closure scheme depending on the turbulent kinetic energy. The parameterization of convection is based on the mass flux concept, in which cumulus clouds are represented by a bulk model including the effects of entrainment and detrainment on both convective updraft and downdraft mass fluxes (Tiedtke1989). The organized entrainment and detrainment are related to in-cloud buoyancy, and an adjusted-type closure is used, which is based on the convective available potential energy (CAPE) with the large-scale moisture convergence as a trigger (Nordeng 1995). We used the T42 resolution corresponding to a horizontal resolution about 2.8°. The model has 19 vertical layers extending from the surface to 10 hPa.

2.3 Coupling strategies

The coupler OASIS (v3.0), developed at the European Centre for Research and Advanced Training in Scientific Computation (CERFACS), France, is used to exchange variables from the atmospheric and oceanic components

(Valcke et al. 2003). Heat flux conservation interpolation is adopted to keep the energy conservation, thereby avoiding the climate drift in the coupled system. Atmosphere and ocean exchange information once a day. The atmosphere model provides daily mean surface wind stress, heat and freshwater fluxes to the ocean model. The latter sends daily mean SST and ocean surface currents back to the former. Ocean surface currents are used to calculate the surface wind stress according to the relative velocity, which could, to a certain degree, eliminate the cold SST bias in the equatorial Pacific (Luo et al. 2005). Currently, the fully coupled region is confined between 60°S and 60°N. Beyond this region, the underlying SST and sea surface ice are specified as the climatological monthly mean derived from the 16-year (1979–1994) dataset, which were used as the boundary conditions in the Atmospheric Model Intercomparison Project (AMIP) II experiments (Taylor et al. 2000).

2.4 Experiments

Several experiments are conducted in this study. The first is a fully coupled run for 100 years after 300 years spinup. Hereinafter we refer to this experiment as the control run (CTRL). In addition, two sensitivity experiments are carried out to demonstrate the potential impact of mean SST bias on ENSO simulation: the annual-mean SST correction (AMSC) run and the ocean-forced (OCN) run. For the AMSC, we use a flux adjustment to 'correct' the annual mean SST field. Briefly, we first carry out a 30-year coupled integration with a strong SST restoring force (a restoring timescale of 5 day) towards the observed climatology, from which the corresponding Newtonian damping term can be estimated and extracted. We, then, average this long-term damping (Fig. 2a) and add it to the SST equation in the coupled AMSC run. Similar to CTRL, we integrate the AMSC for 100 years.

A 50 years' ocean forced run with daily wind stress forcing from the CTRL experiment, and shortwave radiation (SWR) and longwave radiation from the International Satellite Cloud Climatology Project Flux Data (ISCCP-FD) (Zhang et al. 2004), and climatological precipitation from the Global Precipitation Climatology Project (GPCP). Surface winds, air temperature and specific humidity from the National Centers for Environmental Prediction (NCEP) in combination with ocean model SST are used to calculate surface latent and sensible heat fluxes.

2.5 Validation datasets

Several datasets have been used to validate model simulations: Monthly-mean SST (1958–2009) from NOAA Extended Reconstructed SST (ERSST, v3b) (Smith et al. 2008), monthly-mean precipitation (1979–2009) from

GPCP datasets (Adler et al. 2003), surface wind stress (1958–2001) from European Center for Medium-Range Weather Forecasts (ECMWF) Re-Analysis (ERA-40) data (Uppala et al. 2005), and ocean surface heat fluxes (1984–2007) from objectively analyzed air-sea fluxes (OAFlux) (Yu and Weller 2007). A reanalysis of ocean climate using Simple Ocean Data Assimilation (SODA, v2.0.2) is also used (Carton et al. 2005), which is forced by ECMWF surface wind stress from 1958 to 2001. We also used the Climate of the Twentieth Century (20C3 M) simulation from 12 CGCMs from IPCC AR4 (http://www.ipcc-data.org/ar4/scenario-20C3M.html), along with their corresponding available AMIP runs (1980–1999). Table 1 lists all these models along with their brief descriptions.

3 Mean state and ENSO properties

Figure 1 compares the annual mean SST and precipitation over the tropics and extra-tropics obtained from the observations and the CTRL. In most of the ocean basins, SST is simulated reasonably well with realistic spatial patterns. However, a severe warm bias in excess of 1.5°C appears off the western coasts of the America and Africa, which is likely linked to errors in simulating stratus clouds (e.g., Ma et al. 1996) and the marine boundary air-sea feedbacks. A considerable cold SST bias is found in the equatorial Pacific (Fig. 1c), which was suggested to be caused collectively by excessive Bjerknes feedback (Bjerkness 1969), overestimated SST-Latent heat flux (LHF) feedback and insufficient SST-SWR feedback (Lin 2007). Meanwhile, insufficient precipitation occurs over the equatorial western Pacific (WP) and the northern ITCZ (Inter-tropical convergence zone) regions, and excessive precipitation presents over the south of equatorial regions (so-called, the double ITCZ problem). Of particular note is that the largest underprediction (>3 mm/day) is seen in the

WP (Fig. 1f), which may act as a critical factor affecting ENSO simulation by altering air-sea feedbacks in the tropical Pacific. For convenience, we divided the equatorial Pacific into three regions, the WP (west of 180°), equatorial central Pacific (CP, 180°–120°W), and equatorial eastern Pacific (EP, east of 120°W).

As is well known, the growth of ENSO is ascribable to several positive ocean–atmosphere feedbacks that encompass interactions of atmospheric convection, ocean dynamics and the equatorial surface winds (e.g., Jin et al. 2006; Guilyardi et al. 2009b; An et al. 2010). Among them, the most dominant contribution comes from the thermocline feedback, which carries subsurface variability to surface through mean upwelling. The thermocline feedback can be expressed as $-\overline{W}\frac{DT_e}{Dz}$, where $\overline{W}$ represents the equatorial mean upwelling and T_e denotes the subsurface temperature anomaly. Following Jin et al. (2006) and Liu et al. (2011), the thermocline feedback is related to the intensity of, (a) the air-sea coupling strength (R(u, T)) that measures surface wind stress (u) response to SST anomaly (SSTA, T), (b) wind-thermocline coupling (R(Z20, u)) where the 20°C isothermal line (Z20) is used as a proxy of the thermocline depth, (c) thermocline-subsurface temperature coupling (R(Te, Z20)), and (d) mean upwelling ($\overline{W}$).

With an annual-mean Newtonian damping (Fig. 2a), the AMSC rectifies, to a great degree, the SST bias inherent in the coupled system (Fig. 2b). The double ITCZ problem is also largely eliminated compared with the CTRL (Fig. 2c vs. Fig. 1f). In this study, we consider the AMSC to be a best realization although some other fields, such as surface wind stress and precipitation still show non-trivial biases. Figure 3 displays the standard deviation of SSTA from observations, the CTRL and AMSC. In comparison to AMSC, the overall ENSO amplitude in the CTRL does not change much but with a reduced (enhanced) variation over the CP (WP and far EP) (Fig. 3d). Nevertheless, the thermocline feedback in the CTRL is substantially

Table 1 List of models that participate in this study

Modelling group	IPCC ID	Atmospheric resolution	Oceanic resolution
CNRM, France	CNRM-CM3	T63, L45	(0.5°–2°) × 2°, L31
NOAA GFDL, USA	GFDL-CM2.1	2° × 2.5°, L24	(0.3°–1°) × 1°
NASA GISS, USA	GISS-ER	4° × 5°, L20	4° × 5°, L13
IAP, China	FGOALS-g1.0	T42, L26	1° × 1°, L16
INM, Russia	INM-CM3.0	4° × 5°, L21	2° × 2.5°, L33
IPSL, France	IPSL-CM4	2.5° × 3.75°, L19	2° × 2°, L31
CCSR/NIES, Japan	MIROC3.2 (hires)	T106, L56	0.2° × 0.3°, L47
CCSR/NIES, Japan	MIROC3.2 (medres)	T42, L20	(0.5°–1.4°) × 1.4°, L43
MPI, German	ECHAM5/MPI-OM	T63, L31	1.5° × 1.5°, L40
MRI, Janpan	MRI-CGCM2.3.2	T42, L30	(0.5°–2°) × 2.5°, L23
NCAR, USA	CCSM3.0	T85, L26	(0.3°–1°) × 1°, L40
Hadley Center, UK	UKMO-HadGEM1	1.3° × 1.9°, L38	(0.3°–1°) × 1°, L40
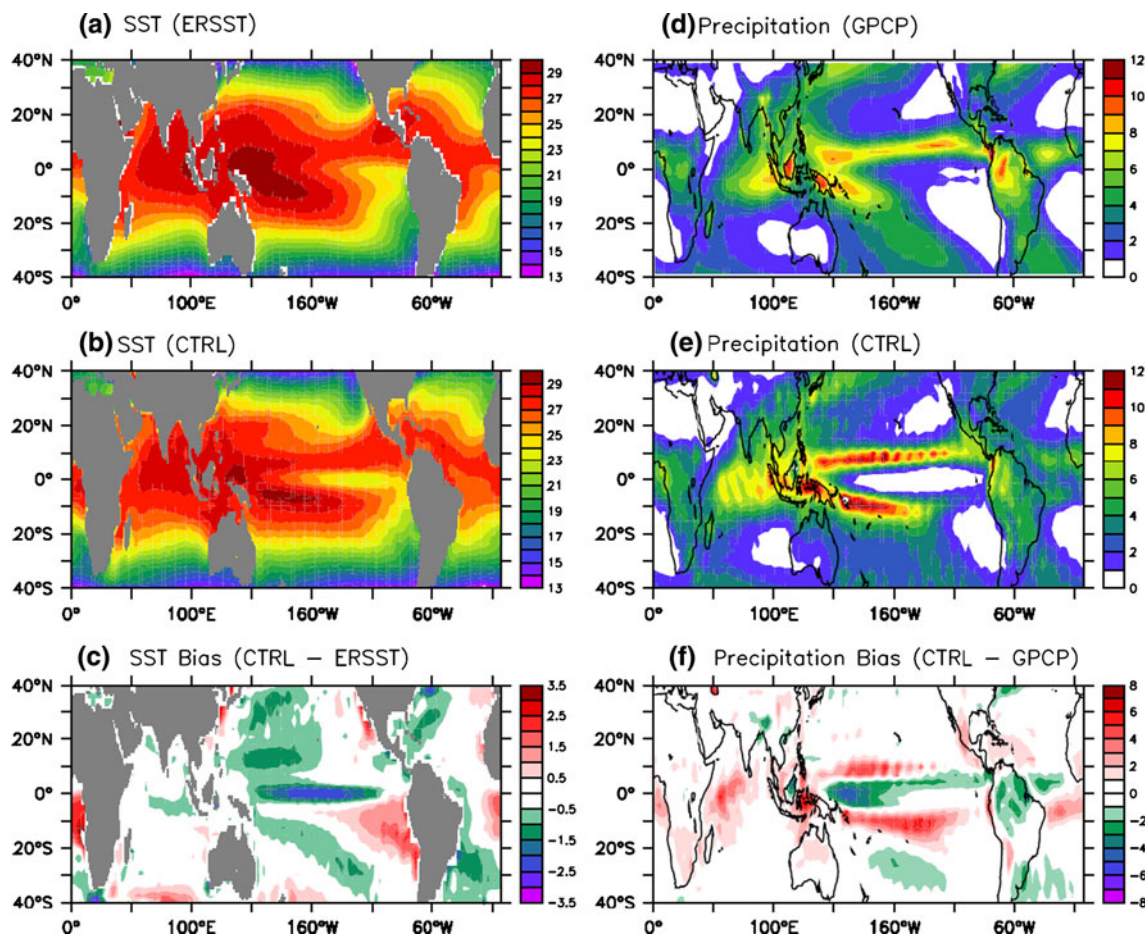
Fig. 1 *Left panel*: Time-mean SST (°C) from **a** ERSST, **b** CTRL, and **c** CTRL–ERSST difference. *Right panel*: Time-mean precipitation (mm day^{-1}) from **d** GPCP, **e** CTRL, and **f** CTRL–GPCP difference

underestimated to be only about 27% of that in the AMSC (Table 2). The weakened thermocline feedback is attributed to the underestimation of air-sea coupling strength (42%), wind-thermocline coupling (16%), thermocline-subsurface temperature coupling (25%) and mean upwelling (27%) (Table 2). We will discuss these four factors in the following several sections.

4 Air-sea coupling strength

Surface zonal wind anomaly acts as an integral component of the Bjerknes feedback that couples the atmospheric anomalous convection and ocean subsurface variability, so that air-sea coupling strength R(u, T) largely determines the intensity of the thermocline feedback. Kim and Jin (2010) found that the majority of current CGCMs underestimate the air-sea coupling strength in comparison to observations. Further, Lioyd et al. (2010) concluded that air-sea coupling strength is usually weaker in coupled runs than in the corresponding AMIP runs. However, the physical explanation is unclear. Here we demonstrate that

the weakened air-sea coupling strength is closely linked to the mean SST bias.

We present, in Fig. 4, the spatial pattern of precipitation and zonal wind stress anomalies that were regressed onto the Niño-3 index from the observations, the CTRL and AMSC. Observational results illustrate that a maximum anomalous precipitation is located near the international dateline, with large portion of precipitation anomaly expanding to the ITCZ region (Fig. 4a). It also indicates that ENSO is strongly convectively coupled with prominent precipitation and surface wind stress anomalies. In the AMSC, ENSO-related maximum precipitation is stronger than that in observations but largely absent in the equatorial EP, so that the resultant zonal wind stress displaces westward (Fig. 4a, c). This is possibly due to the fact that the AMSC still has about 0.5°C cold bias in the EP (Fig. 2b).

However, in the CTRL, ENSO-related precipitation anomaly resembles a horseshoe-like pattern, with two parallel bands of intense precipitation straddling the equator across the equatorial Pacific (Fig. 4b). Note that the CTRL also fails to capture the maximum precipitation anomaly near the international dateline but with a maximum center
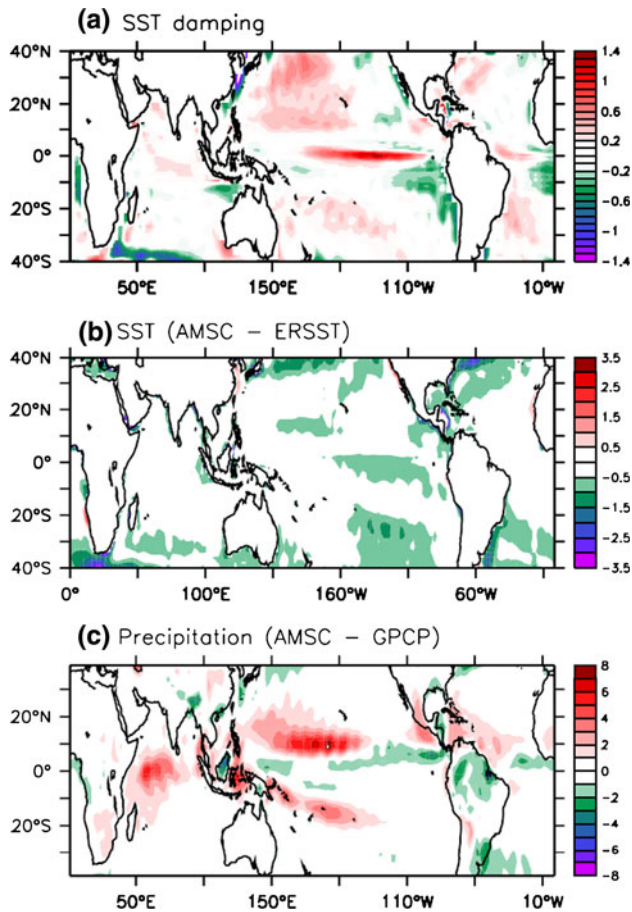
Fig. 2 **a** Horizontal map of the annual mean SST correction term (units: °C per 5 days), time-mean, **b** SST bias (AMSC-ERSST) and **c** precipitation bias (AMSC-GPCP) for the AMSC run

migrating far west. Therefore, when the anomalous convection moves eastward during El Niño events, it tends to move along the zones of warmest SST at 5°S and 5°N, avoiding the cold equatorial region. This bias has direct impacts on the air-sea coupled system with a combination of two effects. First, the suppressed precipitation anomaly, to a great extent, decouples the atmosphere and ocean through reducing the convection-low level wind feedback. Second, the westward displacement of the anomalous convection acts to reduce surface westerly anomaly over the CP. Consequently, surface zonal wind stress anomaly exhibits a zonally elongated but significantly weakened amplitude (Fig. 4b).

Since the maximum zonal wind stress anomaly appears in the CP, we propose to use the zonal wind stress anomaly in the CP, rather than that over the Niño-4 region as Guilyardi et al. (2009a) did, to quantitatively measure the intensity of the air-sea coupling strength. According to this definition, the CTRL produces a much weaker coupling strength than that derived from the AMSC and ERA-40 (Table 2). The air-sea coupling strength is reduced about 42% in the CTRL in comparison to the AMSC. It further

confirms that the errors of coupling strength indeed arise, or at least partly, from the mean SST bias.

To distinguish the convection-induced surface wind anomaly, we use a dry AGCM model which is built based on a dry version of Princeton AGCM with five sigma levels (Jiang and Li 2005; Xiang et al. 2011). This dry AGCM is forced by prescribed heating. It is clear that low-level wind response exhibits distinct patterns with different prescribed mid-tropospheric heating (Fig. 4d–f). For the case with the heating similar to the regressed precipitation pattern from the CTRL, the dry AGCM produces much weaker low level wind anomalies than those from the AMSC and observations. Both from the fully coupled and dry AGCM simulations, one important feature is that the zonal wind stress anomaly related to the precipitation from the CTRL exhibits weak meridional gradient. In the near-equatorial region, the horizontal pressure gradient is weak so that the SST gradient-induced zonal wind is suggested to have weak meridioanl gradient. However, the observational zonal wind anomaly in the CP mainly represents the Rossby wave component with the precipitation heating, which actually decays rapidly in the meridioanl direction. Further, in the CTRL, the maximum zonal wind anomaly is residing to the east of the maximum convection (Fig. 4b). Thus the zonal wind anomaly in the CTRL mainly arises from the zonal SST gradient instead of convective anomaly.

5 Wind-thermocline coupling and thermocline-subsurface temperature coupling

We now focus on another important issue of the thermocline feedback, namely, how the thermocline responds to the surface wind stress forcing and how the subsurface temperature varies with respect to the thermocline depth changes. As is well known, equatorial zonal wind stress forcing can excite eastward propagating Kelvin waves and westward propagating Rossby waves, prompting to form an east–west thermocline contrast pattern. The linear regression of thermocline anomaly regressed onto the CP zonal wind stress anomaly is calculated to estimate the strength of the wind-thermocline coupling R(Z20, u).

We present, in Fig. 5a, b, the thermocline change regressed onto the equatorial zonal wind anomaly averaged over 160°E–130°W, 5°S–5°N. Based on the spatial distribution, the wind-thermocline coupling R(Z20, u) is defined as the regressed thermocline depth averaged over 180°–80°W, 2°S–2°N. Both the AMSC and CTRL obtain weaker wind-thermocline coupling than observations, while the wind-thermocline coupling in the CTRL is weaker about 16% than the AMSC (Table 2). The question arises, however, what causes this weakened wind-thermocline coupling in the CTRL? We argue that this is tightly related
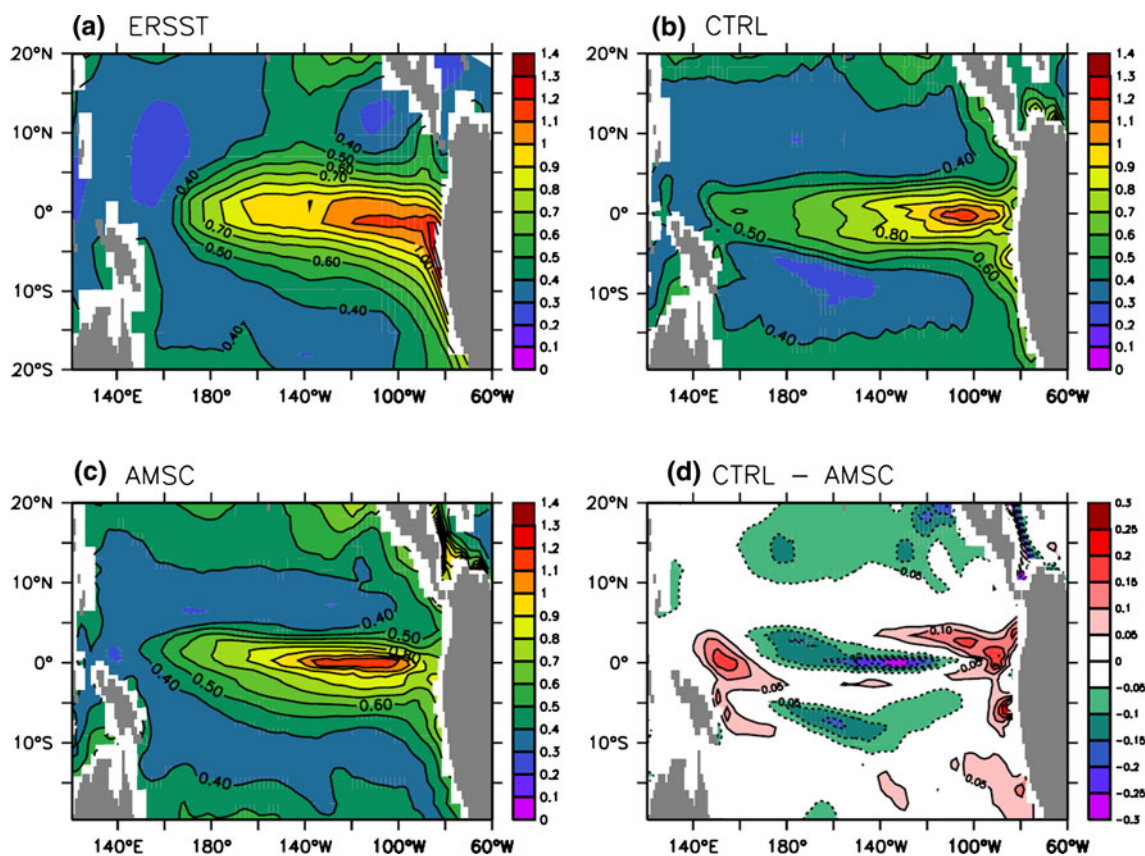
Fig. 3 Standard deviations of SSTA (°C) from **a** ERSST, **b** CTRL, **c** AMSC, **d** CTRL-AMSC

Table 2 Quantitative evaluation of the individual coupling related to the thermocline feedback from observations, AMSC, and CTRL

	R(u, T)	R(Z20, u)	R(Te, Z20)	$\overline{W}$	TH
Observation	10.7	63.2	0.87	1.0	
AMSC	8.1	38.4	1.02	1.13	
CTRL	4.7	32.1	0.76	0.83	
CTRL/AMSC	58%	84%	75%	73%	27%

R(u, T): air-sea coupling strength (10^{-2} dyn cm^{-2}°C^{-1}) measured by the linear regression of equatorial zonal wind stress (160°E–130°W, 5°S–5°N) onto the Niño-3 SSTA; R(Z20, u): thermocline depth (Z20) change (averaged over 180°–80°W, 2°S–2°N) in response to CP (160°E–130°W, 5°S–5°N) surface wind stress forcing (m cm^2 dyn^{-1}); R(Te, Z20): subsurface (60 m) temperature change in response to local Z20 change (averaged over 180°–80°W, 2°S–2°N) (10^{-1}°C m^{-1}); $\overline{W}$: mean upwelling (m day^{-1}) at 60 m averaged over 180°–80°W, 2°S–2°N. TH: the intensity of the thermocline feedback. R(u, T) in observation is estimated from ERA40/ERSST and other couplings in observations are from SODA2.0.2

to the equatorial zonal wind stress pattern (Fig. 5c, d). As mentioned in Sect. 4, the convection-induced westerly anomaly displays strong meridional gradient structure as part of Rossby wave response, however, zonal wind stress in response to zonal SST gradient may have weak meridional gradient. The regressed equatorial (1°S–1°N) zonal wind anomaly averaged over 160°E–130°W is larger in the AMSC than that from the CTRL (1.51 vs. 1.38) although the most intense center from the AMSC shifts to the south of the equator (Fig. 5c, d). Hence, the AMSC attains stronger wind-thermocline coupling since equatorial zonal

wind is more effective to drive equatorial waves than that of the off-equatorial winds.

The wind-induced thermocline depth changes can alter subsurface temperature. We plot the linear regression of equatorial temperature anomaly onto the Z20 anomaly averaged over 180°–80°W, 2°S–2°N (shading in Fig. 6). It can be seen that the CTRL bears close resemblance to the AMSC in representing the maximum temperature changes at the center of the thermocline with strongest mean vertical temperature gradient. Yet, it is significantly weaker at the bottom of the mixed layer depth from the CTRL (shading in
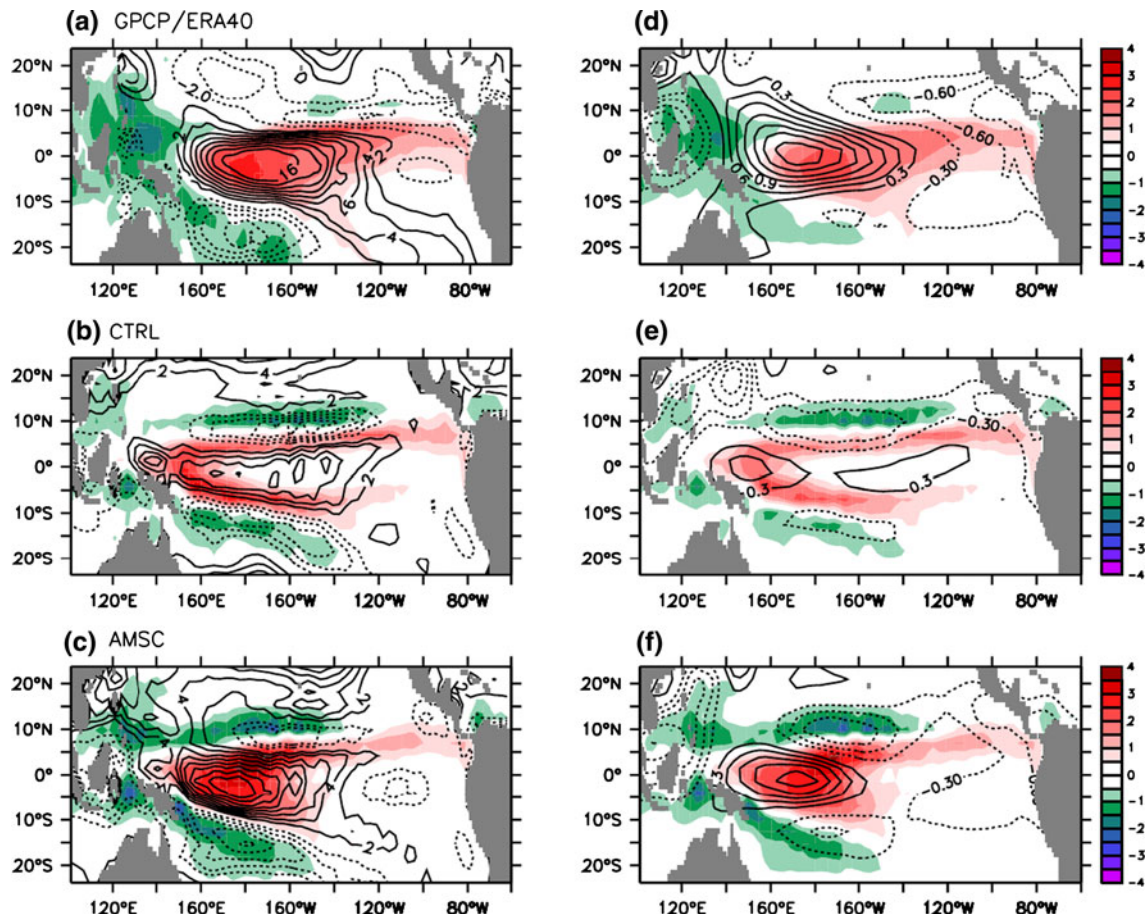
Fig. 4 Precipitation (*shading* in mm day^{-1}°C^{-1}) and surface wind stress (contours in 10^{-2} dyn cm^{-2}°C^{-1}) anomaly regressed onto Niño-3 index from **a** GPCP/ERA40, **b** CTRL, and **c** AMSC. By using a dry AGCM, the right panel (**d–f**) shows the low level wind response (contours in m s^{-1}) to the prescribed mid-tropospheric forcing (K day^{-1}) with the same regressed precipitation pattern from the *left panel*

Fig. 6c). The thermocline-subsurface temperature coupling, R (Te, Z20) is quantitatively measured by the regressed subsurface (60 m) temperature anomaly averaged over 180°–80°W, 2°S–2°N. Results show that R (Te, Z20) in the CTRL is weaker about 25% than that in the AMSC (Table 2). This is attributed to the cold SST bias which induces an underestimation of mean upper-ocean stratification at the bottom of mixed layer (contours in Fig. 6c).

6 Equatorial mean upwelling

6.1 Dynamics determining the equatorial upwelling

Mean equatorial upwelling holds key for ENSO growth, however, it is relatively difficult to measure it directly due to its small magnitude. The equatorial upwelling is usually estimated by calculating the transports of the meridional overturning cell (Johnson et al. 2001; Meinen et al. 2001; Cronin and Kessler 2009) or horizontal divergence.

In the regions away about one Rossby radius ($\sim 2.2°$ latitude) from the equator, the geostrophic and Ekman components are expected to account for the lowest-order dynamics of the near-surface velocity (Lagerloef et al. 1999). In the equatorial Pacific, the meridional geostrophic currents typically show a convergence effect occurring in the upper 200 m, whereas the Ekman currents tend to have a divergence effect within a much shallower depth (Meinen et al. 2001). However, only about half of the Ekman divergence can be counterbalanced by the meridional geostrophic convergence in the upper 50 m. Based on mass conservation, this combination effect from the Ekman divergence and geostrophic convergence necessitates vertical motion with its maximum at the depth around 50 m (Meinen et al. 2001; Johnson et al. 2001).

The divergent Ekman flow, balanced with the Coriolis force and vertical gradient of horizontal viscous force, is by far the largest component contributing to the equatorial upwelling. The meridional Ekman currents can be estimated by:
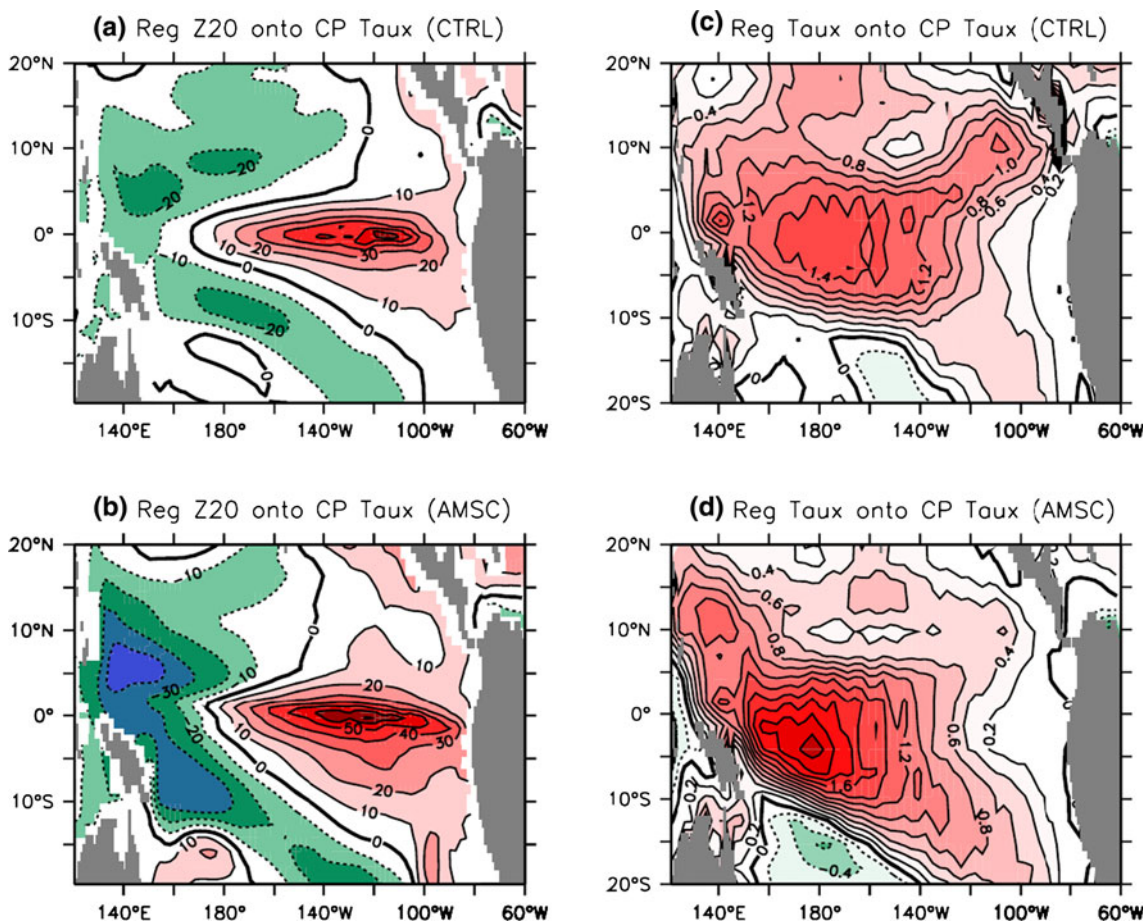
Fig. 5 Thermocline depth (Z20) anomaly regressed onto equatorial zonal wind stress anomaly averaged over 160°E–130°W, 5°S–5°N (in m cm² dyn⁻¹) for the **a** CTRL, **b** AMSC. Zonal wind stress anomaly regressed onto equatorial zonal wind stress anomaly averaged over 160°E–130°W, 5°S–5°N for the **c** CTRL, **d** AMSC

$$-f v_{ek} = \frac{1}{\rho_o} \frac{\partial \tau_x}{\partial z} \qquad (1)$$

where f is the vertical component of the Coriolis parameter, v_{ek} is the meridional Ekman velocity, and ρ_o is the background density. The zonal viscous stress τ_x can be related to the shear profile through the turbulent viscosity parameter A_V,

$$\tau_x(z) = \rho_o A_v \frac{\partial u(z)}{\partial z} \qquad (2)$$

Taking (2) into (1) yields,

$$-f v_{ek} = A_v \frac{\partial^2 u}{\partial z^2}. \qquad (3)$$

The boundary condition can be provided with the balance of the shear stress and surface wind stress τ_o,

$$\tau_{xo} = \rho_o A_v \frac{\partial u}{\partial z} \quad \text{at } z = 0 \qquad (4)$$

$$\tau_{-H} = 0 \quad \text{at } z = -H; \qquad (5)$$

Integrating (1) from the surface to the bottom of the Ekman layer ($-H$) shows that the Ekman transport is to advect waters exactly to the right of the wind stress in the northern hemisphere, to the left in the southern. Although the Ekman transport is only related to the surface wind stress and the Coriolis parameter, the upper ocean Ekman current, especially in the upper 30 m where the poleward divergence is largest (Johnson et al. 2001; Cronin and Kessler 2009), highly depends on the vertical turbulent mixing and the vertical distribution of the zonal currents. Thus, the impacts of mean state biases on the mean upwelling are investigated separately by examining the effects of surface wind stress forcing and interior ocean turbulent mixing.

6.2 Dynamic impacts associated with surface wind stress forcing

Figure 7 displays the longitude-depth diagram of the vertical velocity along the equatorial Pacific from the CTRL
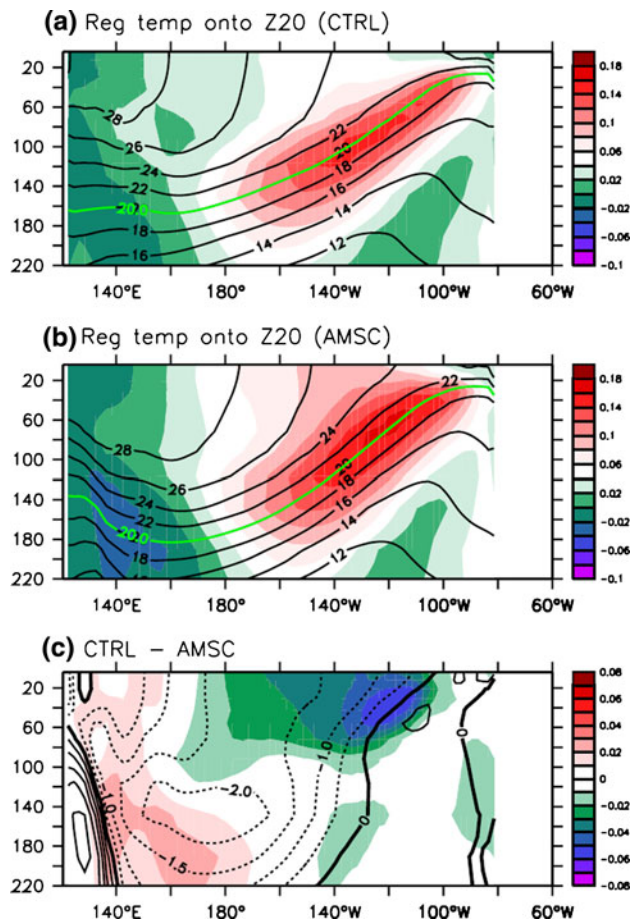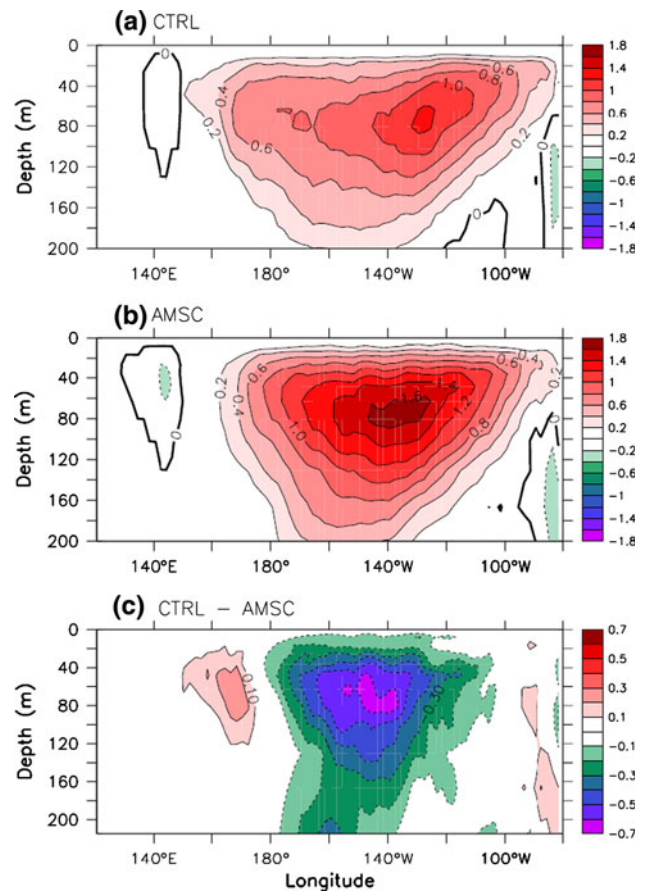
Fig. 6 Equatorial (2°S–2°N) temperature anomaly (*shading* in °C m^{-1}) regressed onto equatorial thermocline depth (Z20) anomaly averaged over 180°–80°W, 2°S–2°N for the **a** CTRL, **b** AMSC, **c** CTRL-AMSC. Contours in the **a**, **b** are the corresponding climatological temperature. Contours in **c** is the climatological temperature difference between the CTRL and AMSC

Fig. 7 Time-mean equatorial (2°S–2°N) upwelling (*shading* in m day^{-1}) from **a** CTRL, **b** AMSC, and **c** CTRL–AMSC difference

and AMSC. For the AMSC, the maximum upwelling is located in the CP around 140°W at the depth of about 60 m (Fig. 7b), with a magnitude of about 1.6 m/day. Compared with AMSC, the CTRL features a substantially weaker upwelling in the CP but slightly stronger upwelling over the WP. The maximum reduction in the CTRL is found at the depth of about 60 m, collocated with AMSC's maximum mean upwelling.

Since the equatorial upwelling velocity is, to the first order approximation, proportional to the intensity of the equatorial easterly wind stress, we examined the surface wind stress difference between these two experiments. Figure 8a shows that the AMSC run has an enhanced (reduced) easterly wind stress in the equatorial CP (WP), which is dynamically consistent with the mean upwelling difference shown in Fig. 7c.

Then, what causes the wind stress difference? Physically, surface wind stress is driven by two different ways,

namely convection and lower boundary SST gradient. In order to identify the responsible mechanisms, we analyzed the mean state differences in sea level pressure (SLP), precipitation and 850 hPa wind between the CTRL and the AMSC (Fig. 8b, c). Note that in the tropical region, the 850 hPa (above the atmospheric boundary layer) wind can be approximately regarded as convectively driven. The surface wind stress and 850 hPa wind differences both show enhanced trades in the equatorial WP, coherent with the underestimated precipitation there. By contrast, large discrepancy appears in the equatorial CP between 850 hPa wind and surface wind stress. At 850 hPa, strong northerly wind is seen in the CP, which is suggestively driven by the excessive precipitation over the south of the equator (Fig. 8c). This is different from surface wind stress difference that shows a large westerly component (Fig. 8b).

This implies that the westerly wind stress difference in the CP (Fig. 8b) is not convectively driven associated with the double ITCZ problem. Actually, it mainly represents a divergent wind component that agrees well with the zonal
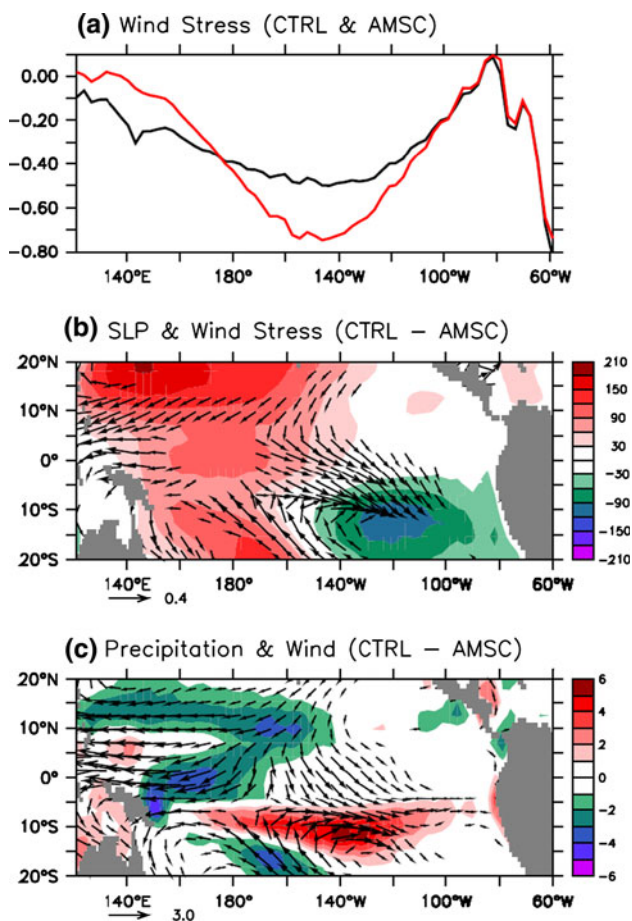
Fig. 8 a Time-mean equatorial (5°S–5°N) zonal wind stress (dyn cm^{-2}) from the CTRL (*black*) and AMSC (*red*). **b** Time-mean differences between CTRL and AMSC of SLP (*shading* in Pa) and surface wind stress (vectors with magnitude greater than 0.1 dyn cm^{-2}), **c** same as **b** but for precipitation (*shading* in mm day^{-1}) and 850 hPa wind (vectors with magnitude greater than 0.4 m s^{-1})

gradients of SLP difference (Fig. 8b). A SLP dipole pattern is apparent with its maximum in the equatorial Pacific around 180°E and minimum in the SEP (Fig. 8b), driving a northwesterly wind with strong westerly component. As such, we argue that this CP wind stress difference primarily originates from the reduced SST zonal gradients (Fig. 1c).

The above arguments highlight the importance of dynamic effects of surface wind stress in determining the intensity of equatorial upwelling. In addition, the thermodynamic effect may also affect the mean upwelling by altering the upper ocean momentum viscosity as well as the Ekman divergence. However, the above comparison between CTRL and AMSC cannot separate these two different processes. In fact, given the same surface wind stress forcing, the equatorial mean upwelling could be different due to the convection-induced mixing in the upper ocean, which is addressed in the next section.

6.3 Thermodynamic impacts associated with upper-ocean convective mixing

As discussed in Sect. 6.1, meridional Ekman divergence plays a dominant role in driving the equatorial upwelling so as to maintain the cold SST in the equatorial EP. To reveal the thermodynamic impacts associated with the excessive cold tongue extension on the equatorial mean upwelling, we compare the CTRL with the OCN. The latter is forced with observed monthly heat and freshwater fluxes, but with daily wind stress forcing from the output of the CTRL. Thus, the model difference between them must originate from heat and/or freshwater fluxes forcing. The purpose to use daily wind stress forcing for the OCN is to retain high frequency wind variability which may substantially influence the upper ocean vertical mixing.

Compared with the OCN, the CTRL also displays pronounced SST cooling between 160°E and 120°W with its maximum cooling of about −1.5°C near 160°W (Fig. 9a). Consistently, a deepened mixed layer is evident over the equatorial region (Fig. 9b). In terms of the mean upwelling, the CTRL exhibits a prominently underestimated upwelling in the region generally collocated with the region of pronounced SST cooling (Fig. 9c). One striking feature is that the reduced upwelling is located in a relatively shallower depth compared with the case mainly due to the dynamic wind stress forcing effect (Fig. 9c vs. Fig. 7c).

To understand the cause of this, we present the meridional currents averaged in the upper 30 m (Fig. 10a, b). Clearly, the CTRL experiment has much weaker meridional currents and features weaker meridional gradient in the region between 160°E and 130°W. Meanwhile, a baroclinic structure with near-surface divergence and subsurface convergence is evident in the vertical-meridional diagram of the mean meridional currents averaged over 160°E–130°W. The difference between the CTRL and OCN (contours in Fig. 10d) illustrates an opposite structure to the mean pattern with near surface convergence and subsurface divergence indicating weaker divergence in CTRL (Fig. 10c). This meridioanl current difference readily accounts for the weaker upwelling in the CP in the CTRL.

Since these two experiments share the same daily wind stress forcing, the meridional currents difference should originate from thermodynamic effect related to the upper-ocean buoyancy. From the definition of Ekman currents (3), vertical mixing acts as a necessary condition to produce Ekman currents as well as upwelling. However, cold SST bias could enhance the convective eddy-induced mixing and turbulent viscosity, which also reduces the vertical shear of currents because currents with strong vertical shear can only come out the region with stable stratification.
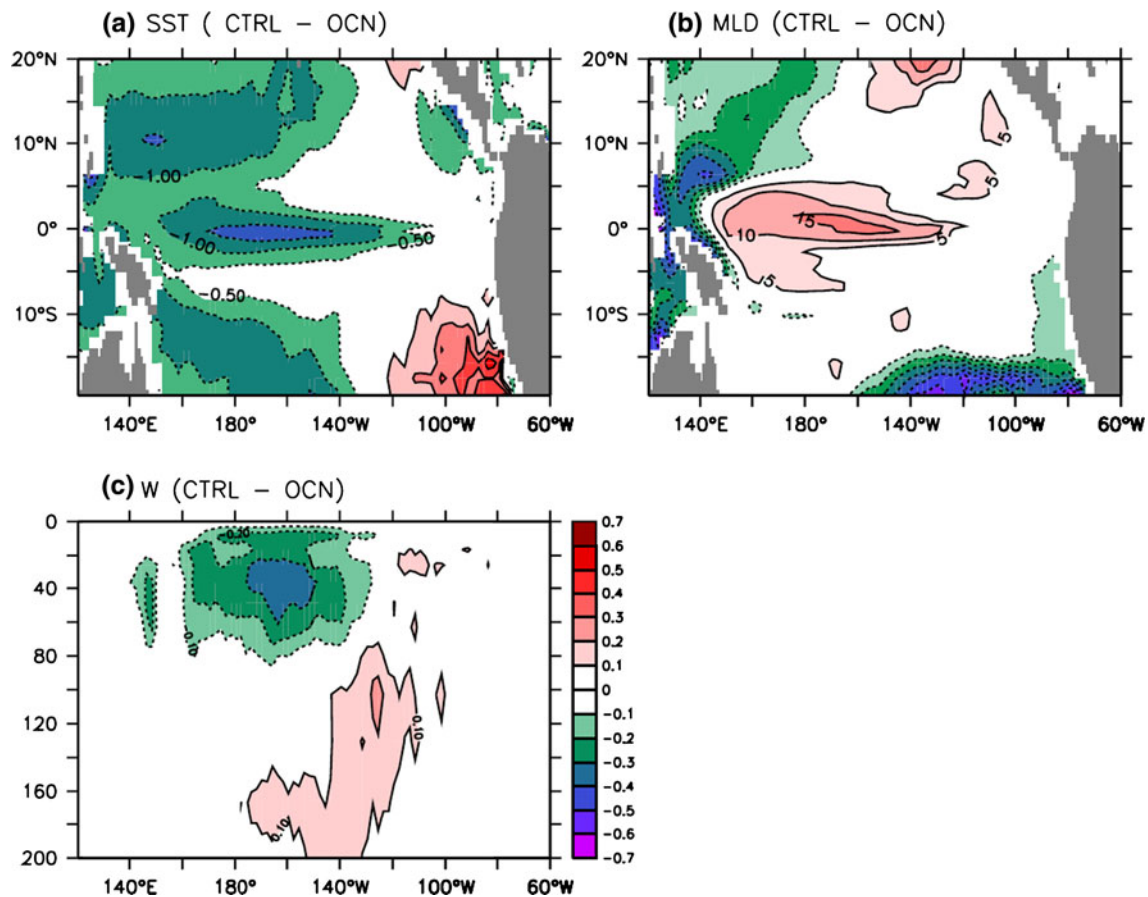
Fig. 9 a Time-mean difference of **a** SST (°C), **b** mixed layer depth (m), and **c** equatorial (2°S–2°N) mean upwelling (m day^{-1}) differences between CTRL and OCN

Results also show that sea surface height (SSH) patterns derived from these two experiments are very similar (not shown), indicating that the convergent geostrophic currents are almost identical. As a result, the meridioanl currents difference mentioned above should be attributed to Ekman currents. To help visulizing a more complete picture, we plot the zonally (160°E–130°W) averaged mean viscous stress along 2.8°N and 2.8°S (Fig. 11). As expected, the zonal viscous stress is stronger in the upper ocean in the CTRL, except at sea surface where it is identical to surface wind stress. The maximum of the intensified viscous stress is residing at the depth of about 30 m (Fig. 11), leading to a reduced (increased) vertical shear of zonal viscous stress in the depth range above (below) 30 m. Based on the viscous stress, we further estimate the meridional Ekman currents. The CTRL depicts weaker meridional Ekman currents at the depth above 30 m but stronger below this (Fig. 12), which is responsible for generating a weakened upwelling shown in Fig. 9c.

7 Summary and discussions

Although contemporary climate models have achieved substantial improvements in ENSO simulation (Latif et al. 2001; AchutaRao and Sperber 2002; Meehl et al. 2005; Randall et al. 2007), great challenges remain in many aspects. The thermocline feedback serves as the most dominant process for the development of ENSO, however, the majority of current CGCMs exhibit underestimated thermocline feedback (Kim and Jin 2010). Mean state biases inherent in the current CGCMs could be one alternative candidate for the underestimation of thermocline feedback. Thus, understanding the impact of the systematic biases On ENSO is instrumental for finding the causes of the deficiencies and improving ENSO simulation.

Associated with the double ITCZ problem, mean SST bias typically resembles a dipole pattern with excessive cold tongue extension in the equatorial CP and excessive warm SST in the SEP. This is a long standing and challenging issue inherent in many contemporary CGCMs.
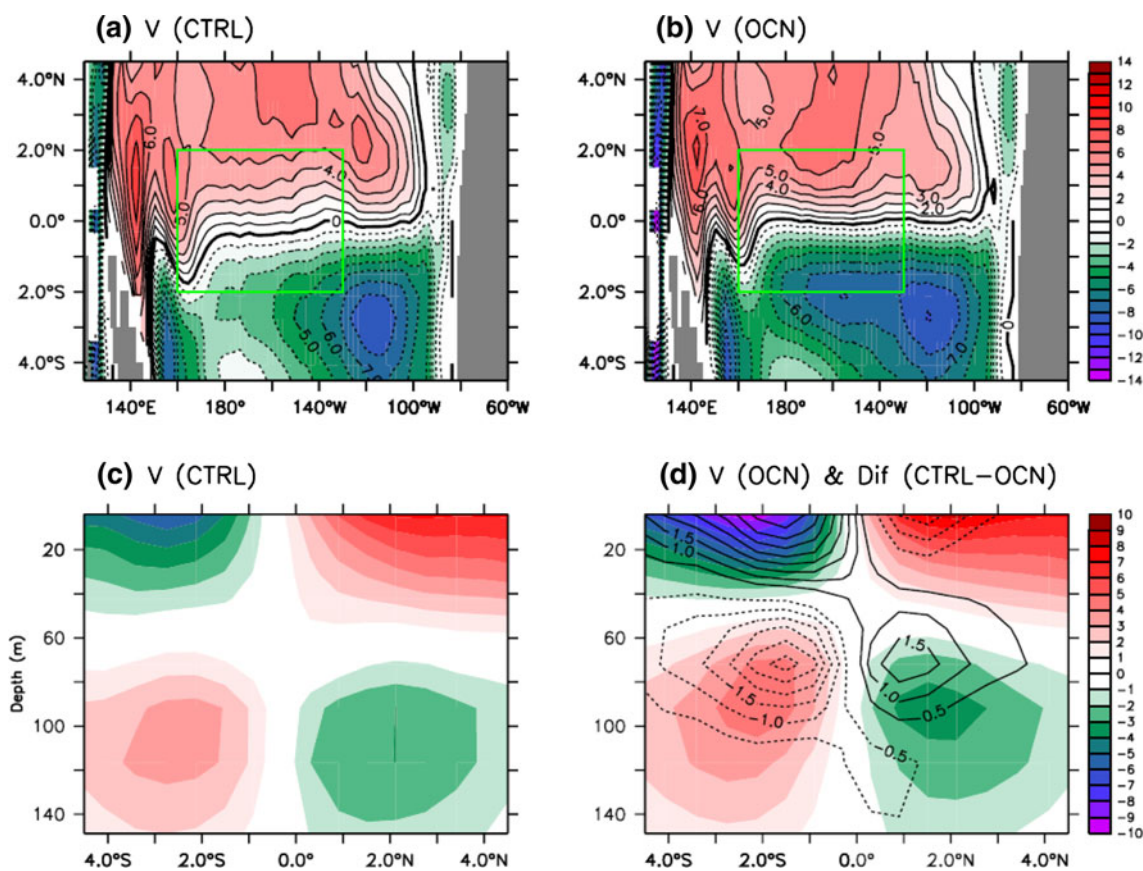
Fig. 10 Time-mean meridional currents (cm s^{-1}) averaged over the upper 30 m from **a** CTRL, **b** OCN. Vertical-Longitudinal diagram of time-mean meridional currents averaged over 160°E–130°W from **c** CTRL, **d** OCN. Contours in **d** indicate the corresponding meridional currents difference between CTRL and OCN


Fig. 11 Time-mean horizontal viscous stress (cm^2 s^{-2}) averaged over 160°E–130°W along **a** 2.8°N and **b** 2.8°S. The *black* and *red lines* indicate the results from the CTRL and OCN experiments, respectively. The *green line* shows the difference between CTRL and OCN
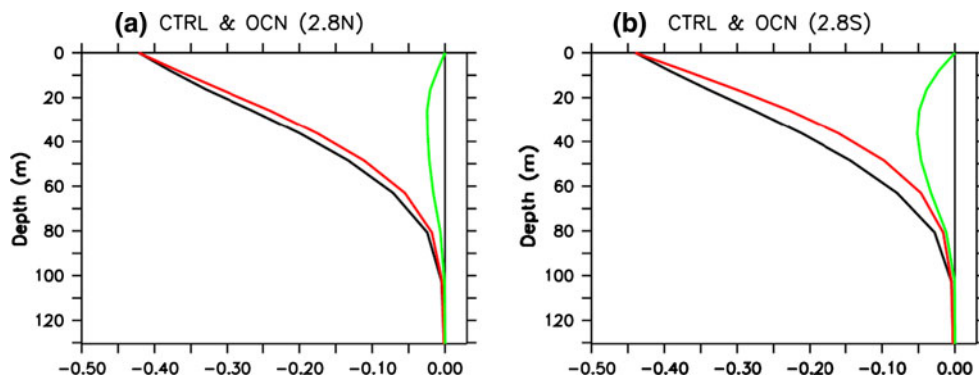
Based on a newly-developed coupled model—POEM, we revealed that this systematic SST bias can severely suppress the thermocline feedback, through reducing the air-sea coupling strength, wind-thermocline coupling, thermocline-subsurface temperature coupling and equatorial mean upwelling.

Firstly, the equatorial cold SST bias weakens and pushes the mean Walker circulation westward, which leads to a significant underestimati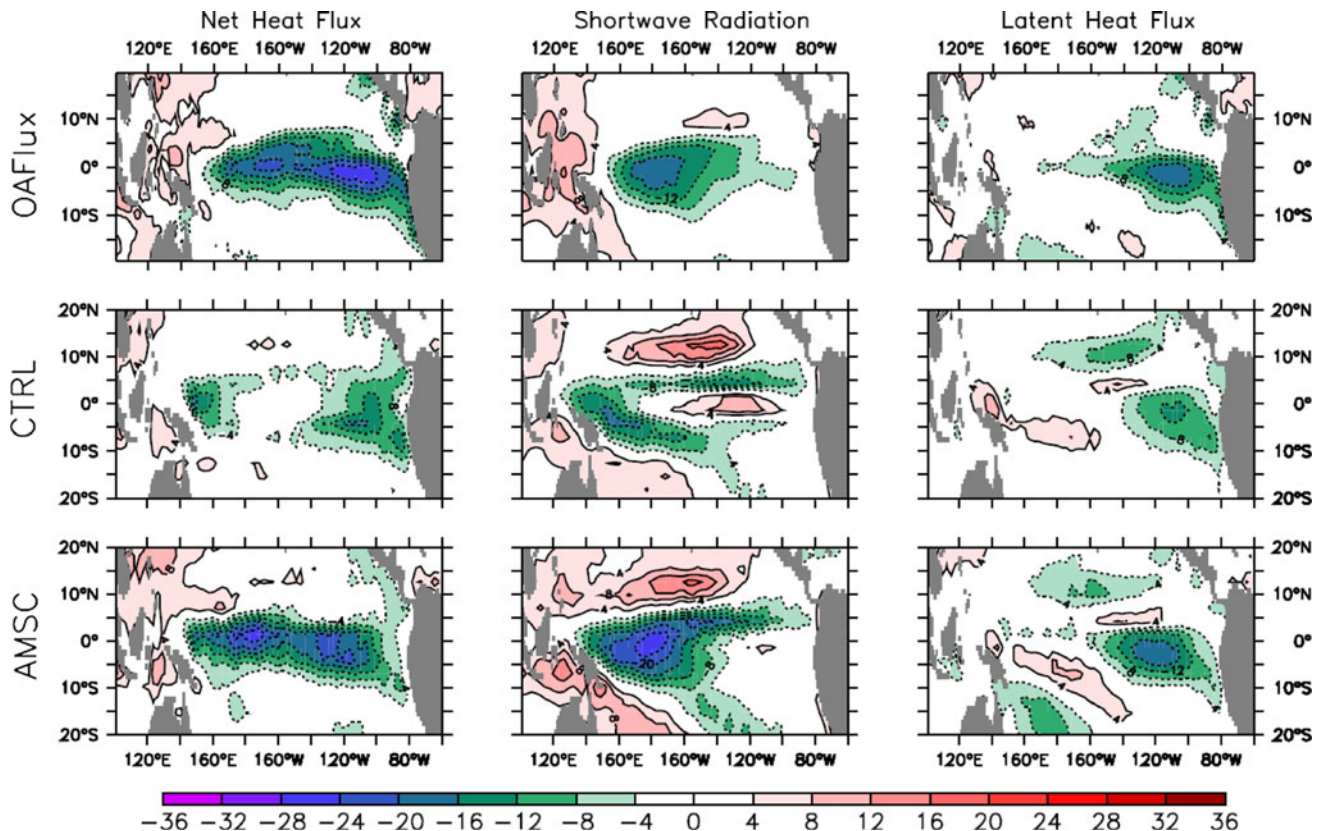on of convection-low level wind feedback as well as air-sea coupling strength. Secondly, with the suppression of anomalous deep convection over the CP, the equatorial surface zonal wind anomaly exhibits weak meridional gradient that is suggestively responsible for the underestimated wind-thermocline coupling. Thirdly, equatorial cold SST bias leads to a weakened mean stratification, yielding a reduced thermocline-subsurface temperature feedback. Finally, both dynamic and thermodynamic effects from this SST bias contribute to the
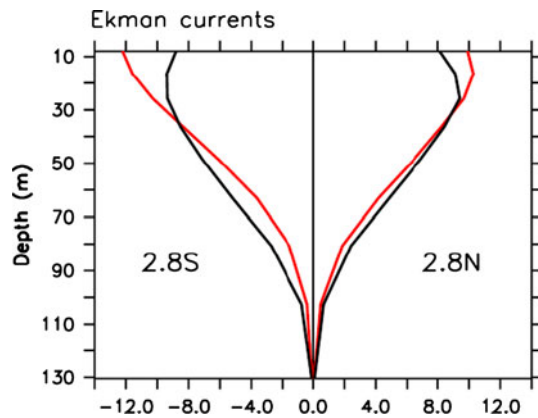
Fig. 12 Estimated meridional Ekman currents (cm s^{-1}) averaged over 160°E–130°W from CTRL (*black*) and OCN (*red*) along 2.8°S and 2.8°N, based on the zonal viscous stress shown in Fig. 11

One intriguing feature is that although the thermocline feedback is largely underestimated, the simulated ENSO amplitude in the CTRL is comparable with that in the AMSC. We argued that the decrease of thermal damping effect largely compensates the effect of the reduced thermocline feedback. The SWR and LHF feedbacks are two dominant components for the thermal damping (Jin et al. 2006). Thermal damping can be measured by the heat flux anomaly (net, SWR, LHF) regressed onto Niño-3 SSTA (Fig. 13). Observational results show that SWR feedback dominates over LHF feedback in the region between 140°E and 140°W, and the opposite is true in the region east of 140°W. Different CGCMs show large diversity in thermal damping particularly due to large uncertainty in SWR feedback (Lioyd et al. 2010; Kim and Jin 2010). Strikingly, the AMSC realistically captures both the SWR and LHF feedbacks, whereas these feedbacks are significantly underestimated in the CTRL. The weak SWR feedback in the CTRL can be a consequence of the weakened anomalous convection together with its maximum center migrating westward. The reduced LHF feedback is conceivable to be ascribed to the reduced mean southeasterly trade wind speed (Fig. 8b) and lower specific humidity associated with cold SST bias.

weakened mean equatorial upwelling. The dynamic effect arises from the weakened easterly wind stress in the CP because of the reduced east–west zonal SST gradient. Meanwhile, the equatorial cold SST bias considerably enhances the upper-ocean vertical mixing but reduces the vertical shear of meridional currents, resulting in a weakened upper ocean Ekman divergence and mean upwelling.

Fig. 13 Thermal damping measured by the monthly heat flux anomaly regressed onto Niño-3 SSTA for observations (*upper*), CTRL (*middle*) and AMSC (*bottom*). The *left panel* is for net heat flux, the *middle* for shortwave radiation and *right panel* for latent heat flux. Units: W m^{-2}°C^{-1}
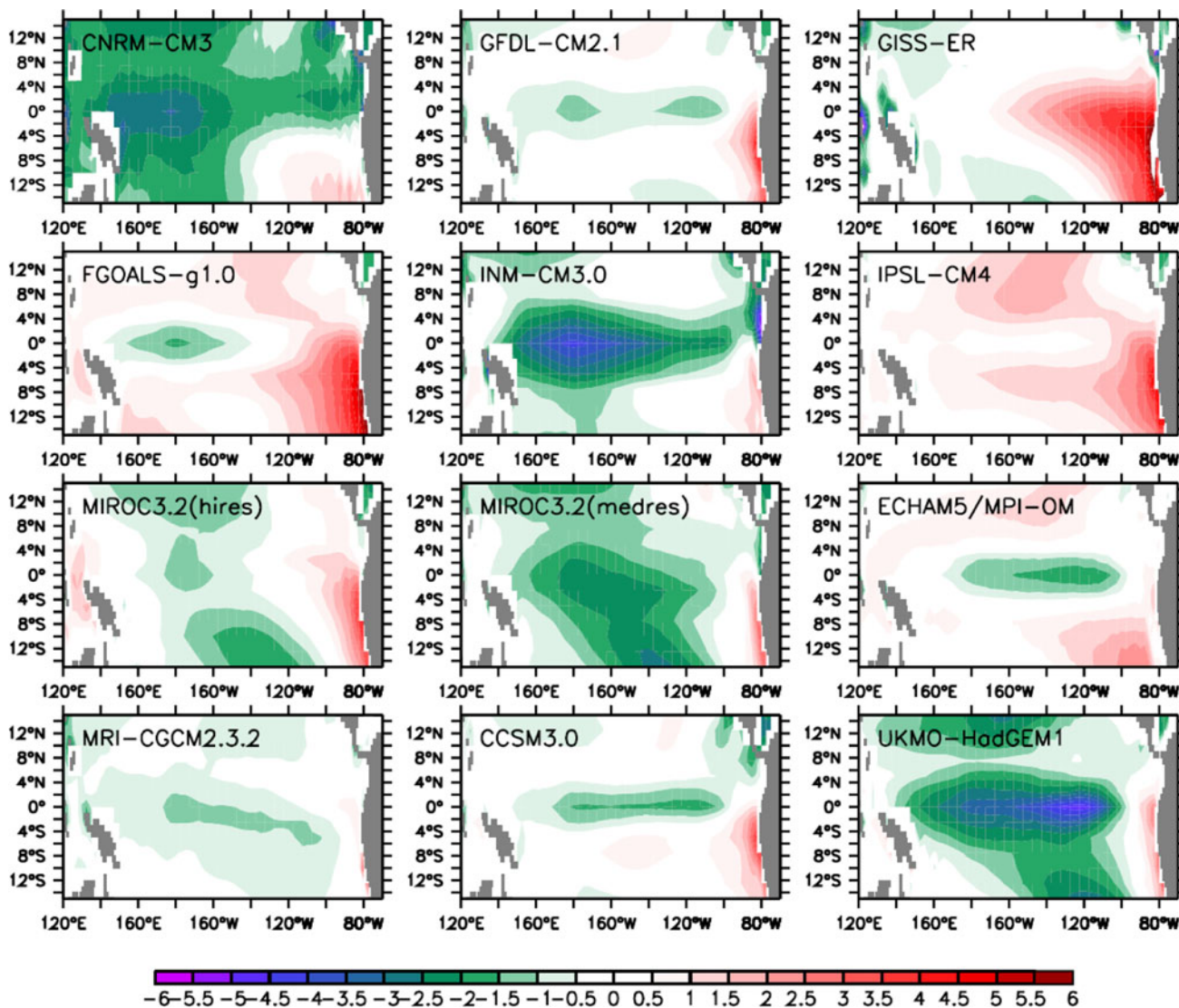
Fig. 14 The SST bias (°C) from 12 CGCMs in comparison to the ERSST climatology. The period 1980–1999 is chosen to be consistent with the AMIP runs

How does the SST bias influence the ENSO amplitude may be model-dependent, as the ENSO amplitude also relies on some other processes, such as the zonal advection feedback, nonlinearity (e.g., An 2008) and noise level (e.g., Zavala-Garay et al. 2003; Jin et al. 2007). Nevertheless, those processes affecting the thermocline feedback proposed in this study are suggested to be applicable for other CGCMs. For example, we investigated 12 CGCMs from IPCC AR4 together with their corresponding AMIP runs (Table 1). The results show that most of them have cold SST bias in the CP and WP and warm bias in the SEP (Fig. 14), and the accompanying excessive (underestimated) easterly wind is evident in the far WP (CP) (Fig. 15). Therefore, the upwelling bias due to the dynamic

surface wind stress is expected to be a common problem for current state-of-the-art CGCMs. The thermodynamic effect is also bound to influence the mean upwelling, particularly for those with serious cold SST bias in the equatorial Pacific.

Atmosphere–ocean mean state biases will result in serious problems in representing the ENSO simulation in CGCMs. Thus, a prerequisite to have reasonable and realistic ENSO simulation is to get a realistic annual-mean state. Considerable efforts have been made to alleviate the double ITCZ problem in current CGCMs, through modifications of atmospheric cumulus parameterizations (Kim et al. 2008; Song and Zhang 2009), upper ocean stratification by considering diurnal cycle effects (Danabasoglu
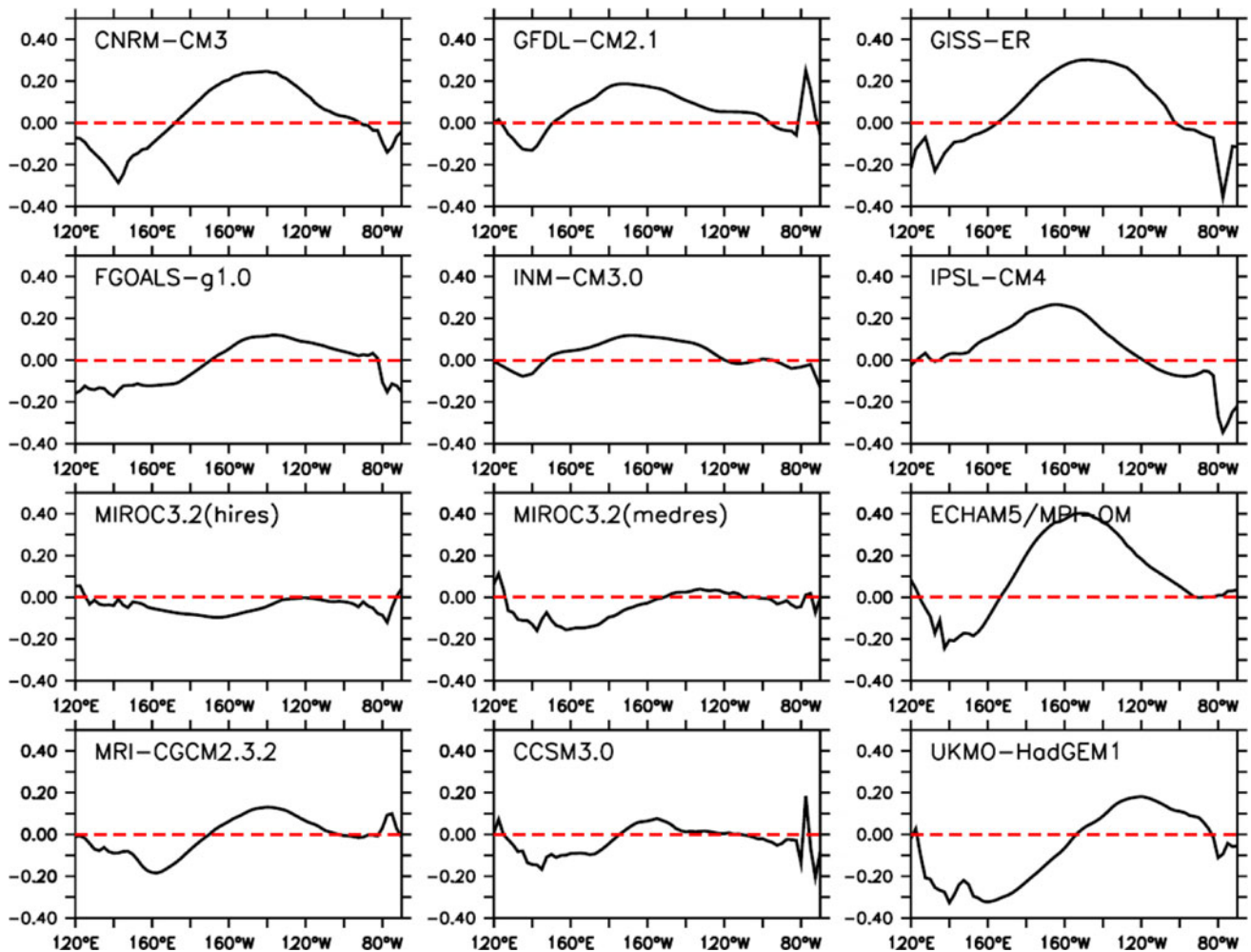
Fig. 15 The equatorial (5°S–5°N) zonal wind stress (dyn cm^{-2}) differences between the fully coupled runs and AMIP runs

et al. 2006), and so on. Yet, reducing the systematic biases in CGCMs still remains a thorny and challenging issue.

References

AchutaRao K, Sperber K (2002) Simulation of the El Niño Southern Oscillation: results from the coupled model intercomparison project. Clim Dyn 19:191–209

AchutaRao K, Sperber K (2006) ENSO simulation in coupled ocean-atmosphere models: are the current models better? Clim Dyn 27:1–16

Adler RF et al (2003) The version-2 global precipitation climatology project (GPCP) monthly precipitation analysis (1979-present). J Hydrometeor 4:1147–1167

An S-I (2008) Interannual variations of the tropical ocean instability wave and ENSO. J Clim 21:3680–3686

An S-I, Jin F–F (2001) Collective role of thermocline and zonal advective feedbacks in the ENSO mode. J Clim 14:3421–3432

An S-I, Ham Y-G, Kug J-S, Timmermann A, Choi J, Kang I-S (2010) The inverse effect of annual-mean state and annual-cycle changes on ENSO. J Clim 23:1095–1110

Bjerknes J (1969) Atmospheric teleconnections from the equatorial Pacific. Mon Wea Rev 97:163–172

Carton JA, Giese BS, Grodsky SA (2005) Sea level rise and the warming of the oceans in the SODA ocean reanalysis. J Geophys Res 110. doi:10.1029/2004JC002817

Cronin MF, Kessler WS (2009) Near-Surface shear flow in the tropical Pacific cold tongue front. J Phys Oceanogr 39:1200–1215

Danabasoglu G, Large WG, Tribbia JJ, Gent PR, Briegleb BP (2006) Diurnal coupling in the tropical oceans of CCSM3. J Clim 19:2347–2365

Dukowicz JK, Smith RD (1994) Implicit free-surface method for the bryan-cox-semtner ocean model. J Geophys Res 99:7991–8014

Fedorov AV, Philander SGH (2000) Is El Niño changing? Science 288:1997–2002

Gent PR, McWilliams JC (1990) Isopycnal mixing in ocean circulation models. J Phys Oceanogr 20:150–155

Guilyardi E (2006) El Niño-mean state-seasonal cycle intearactions in a multi-model ensemble. Clim Dyn 26:329–348

Guilyardi E, Braconnot P, Jin F–F, Kim ST, Kolasinski M, Li T, Musat I (2009a) Atmosphere feedbacks during ENSO in a coupled GCM with a modified atmospheric convection scheme. J Clim 22:5698–5718

Guilyardi E, Wittenberg A, Fedorov A, Collins M, Wang C, Capotondi A, Oldenborgh GJV, Stockdale T (2009b) Understanding El Niño in ocean-atmosphere general circulation models. Bull Am Meteor Soc 90:325–340

Guldberg A, Kaas E, Deque M, Yang S, Vester TS (2005) Reduction of systematic errors by empirical model correction impact on seasonal prediction skill. Tellus 57A:575–588

Jiang X, Li T (2005) Re-initiation of the boreal summer intraseasonal oscillation in the tropical Indian Ocean. J Clim 18:3777–3795

Jin F–F, Kim ST, Bejarano L (2006) A coupled stability index for ENSO. Geophys Res Lett 33:L23708. doi:101029/2006GL027221

Jin F–F, Lin L, Timmermann A, Zhao J (2007) Ensemble-mean dynamics of the ENSO recharge oscillator under state-dependent stochastic forcing. Geophys Res Lett 34:L03807. doi:10.1029/2006GL027372

Johnson GC, McPhaden MJ, Firing E (2001) Equatorial Pacific Ocean horizontal velocity, divergence, and upwelling. J Phys Oceanogr 31:839–849

Joseph R, Nigam S (2006) ENSO evolution and teleconnections in IPCC's twentieth-century climate simulations Realistic representation? J Clim 19:4360–4377

Kim ST, Jin F–F (2010) An ENSO stability analysis Part II: results from the twentieth and twenty-first century simulations of the CMIP3 models. Clim Dyn. doi:101007/s00382-010-0872-5

Kim D, Kug J-S, Kang I-S, Jin F–F, Wittenberg AT (2008) Tropical Pacific impacts of convective momentum transport in the SNU coupled GCM. Clim Dyn 31:213–226

Lagerloef GSE, Mitchum GT, Lukas RB, Niller PP (1999) Tropical Pacific near-surface currents estimated from altimeter, wind, and drifter data. J Geophys Res 104(C10):23313–23326

Large WG, Danabasoglu G (2006) Attribution and impacts of upper-ocean biases in CCSM3. J Clim 19:2325–2346

Large WG, McWilliams JC, Doney SC (1994) Oceanic vertical mixing a review and a model with a nonlocal boundary layer parameterization. Rev Geophys 32:363–403

Large WG, Danabasoglu G, Doney SC, McWilliams JC (1997) Sensitivity to surface forcing and boundary layer mixing in a global ocean model annual-mean climatology. J Phys Oceanogr 27:2418–2447

Latif M, Keenlyside NS (2009) El Niño/Southern Oscillation response to global warming. PNAS 106:20578–20583

Latif M et al (2001) ENSIP: the El Niño simulation intercomparision project. Clim Dyn 18:255–276

Li T, Hogan TF (1999) The role of annual-mean climate on seasonal and interannual variability of the tropical Pacific in a coupled GCM. J Clim 12:780–792

Lin J-L (2007) The double-ITCZ problem in IPCC AR4 coupled GCMs Ocean-Atmosphere feedback analysis. J Clim 20:4497–4525

Lioyd J, Guilyardi E, Weller H (2010) The role of atmosphere feedbacks during ENSO in the CMIP3 models part II using AMIP runs to understand the heat flux feedback mechanisms. Clim Dyn. doi:101007/s00382-010-0895-y:

Liu L, Yu W, Li T (2011) Dynamic and thermodynamic air-sea coupling associated with the Indain Ocean dipole diagnosed from 23 WCRP CMIP3 models. J Clim. doi:10.1175/2011JCLI4041.1

Luo J–J, Masson S, Roeckner E, Madec G, Yamagata T (2005) Reducing climatology bias in an ocean-atmosphere CGCM with improved coupling physics. J Clim 18:2344–2360

Ma C–C, Mechoso CR, Robertson AW, Arakawa A (1996) Peruvian stratus clouds and tropical Pacific circulation a coupled ocean-atmosphere GCM study. J Clim 9:1635–1645

Manganello JV, Huang B (2009) The influence of systematic errors in the Southeast Pacific on ENSO variability and prediction in a coupled GCM. Clim Dyn. doi:101007/s00382-008-0407-5

Mechoso CR et al (1995) The seasonal cycle over the tropical Pacific in coupled ocean-atmosphere general circulation models. Mon Wea Rev 123:2825–2835

Meehl GA, Gent PR, Arblaster JM, Otto-Bliesner BL, Brady EC, Craig A (2001) Factors that affect the amplitude of El Niño in global coupled climate models. Clim Dyn 17:515–526

Meehl GA, Covey C, McAvaney B, Latif M, Stouffer RJ (2005) Overview of the coupled model intercomparison project. Bull Am Meteor Soc 86:89–93

Meinen CS, McPhaden MJ, Johnson GC (2001) Vertical velocities and transports in the Equatorial Pacific during 1993–99. J Phys Oceanogr 31:3230–3248

Merryfield WJ (2006) Changes to ENSO under CO2 doubling in a multimodel ensemble. J Clim 19:4009–4027

Neale RB, Richter JH, Jochum M (2008) The impact of convection on ENSO: from a delayed oscillator to a series of events. J Clim 21:5904–5924

Nordeng TE (1995) Extended versions of the convective parameterization scheme at ECMWF and their impact on the mean and transient activity of the model in the tropics ECMWF Research Dept Tech Memo, 206, European Centre for Medium-Range Weather Forecasts, Reading, United Kingdom, 41 pp

Ohlmann JC (2003) Ocean radiant heating in climate models. J Clim 16:1337–1351

Philip SY, Van Oldenborgh GJ (2006) Shifts in ENSO coupling processes under global warming. Geophys Res Lett 33:L11704. doi:10.1029/2006GL026196

Randall DA, et al (2007) Climate models and their evaluation. In: Solomon S et al. (eds) Climate change 2007: the physical science basis. Cambridge University Press, Cambridge, pp 589–662

Roeckner E et al. (1996) The atmospheric general circulation model ECHAM-4: model description and simulation of present-day climate. Max-Planck-Institute for Meteorology Rep 218, 90 pp

Smith RD, Dukowicz JK, Malone RC (1992) Parallel ocean general circulation modeling. Physica D 60:38–61

Smith TM, Reynolds RW, Peterson TC, Lawrimore J (2008) Improvements to NOAA's historical merged land-ocean surface temperature analysis (1880–2006). J Clim 21:2283–2293

Song X, Zhang GJ (2009) Convection parameterization, Tropical Pacific double ITCZ, and upper-ocean biases in the NCAR CCSM3. Part I: climatology and atmospheric feedback. J Clim 22:4299–4315

Spencer H, Sutton R, Slingo JM (2007) El Niño in a coupled climate model sensitivity to changes in mean state induced by heat flux and wind stress corrections. J Clim 15:2273–2298

Taylor KE, Williamson D, Zwiers F (2000) The sea surface temperature and sea-ice concentration boundary condition for AMIP II simulations, PCMDI Rep 60, Program for Climate Model Diagnosis and Intercomparison, Lawrence Livermore National Laboratory, Livermore, CA, 25 pp

Tiedtke M (1989) A comprehensive mass flux scheme for cumulus parameterization in large-scale models. Mon Wea Rev 117:1779–1800

Uppala SM et al (2005) The ERA-40 Re-analysis. Quart J Roy Meteor Soc 131:2961–3012

Valcke S, Caubel A, Declat D, Terry L (2003) OASIS3 ocean atmosphere sea ice soil user's guide tech rep TR/CMGC/03/69, CERFACS, Toulouse, France, 57 pp

Vitart F, Balmaseda MA, Ferranti L, Anderson D (2003) Westerly wind events and the 1997/98 El Niño event in the ECMWF seasonal forecasting system: a case study. J Clim 16:3153–3170

Wang B, An S-I (2001) Why the properties of El Niño changed during the late 1970s. Geophys Res Lett 28:3709–3712

Wittenberg AT, Rosati A, Lau N-C, Ploshay JJ (2006) GFDL's CM2 global coupled climate models part III tropical pacific climate and ENSO. J Clim 19:698–722

Xiang B, Yu W, Li T, Wang B (2011) The critical role of the boreal summer mean state in the development of the IOD. Geophys Res Lett 38:L02710. doi:10.1029/2010GL045851

Yeager SG, Shields CA, Large WG, Hack JJ (2006) The low-resolution CCSM3. J Clim 19:2545–2566

Yu L, Weller RA (2007) Objectively analyzed air-sea heat fluxes for the global oce-free oceans (1981–2005). Bull Am Meteor Soc 88:527–539

Zavala-Garay J, Moore AM, Perez CL, Kleeman R (2003) The response of a coupled model of ENSO to observed estimates of stochastic forcing. J Clim 16:2827–2842

Zhang Y, Rossow WB, Lacis AA, Oinas V, Mishchenko MI (2004) Calculation of radiative fluxes from the surface to top of atmosphere based on ISCCP and other global data sets: refinements of the radiative transfer model and the input data. J Geophys Res 109:D19105. doi:101029/2003JD004457